# Visibility graphs of random scalar fields and spatial data

Lucas Lacasa* and Jacopo Iacovacci†
*School of Mathematical Sciences, Queen Mary University of London, Mile End Road, London E14NS, United Kingdom*
(Received 30 March 2017; revised manuscript received 28 May 2017; published 21 July 2017)

We extend the family of visibility algorithms to map scalar fields of arbitrary dimension into graphs, enabling the analysis of spatially extended data structures as networks. We introduce several possible extensions and provide analytical results on the topological properties of the graphs associated to different types of real-valued matrices, which can be understood as the high and low disorder limits of real-valued scalar fields. In particular, we find a closed expression for the degree distribution of these graphs associated to uncorrelated random fields of generic dimension. This result holds independently of the field's marginal distribution and it directly yields a statistical randomness test, applicable in any dimension. We showcase its usefulness by discriminating spatial snapshots of two-dimensional white noise from snapshots of a two-dimensional lattice of diffusively coupled chaotic maps, a system that generates high dimensional spatiotemporal chaos. The range of potential applications of this combinatorial framework includes image processing in engineering, the description of surface growth in material science, soft matter or medicine, and the characterization of potential energy surfaces in chemistry, disordered systems, and high energy physics. An illustration on the applicability of this method for the classification of the different stages involved in carcinogenesis is briefly discussed.

DOI: 10.1103/PhysRevE.96.012318

## I. INTRODUCTION

The concept of visibility graphs was introduced in computational geometry and graph theory some decades ago in order to abstract the intervisible structure of a set of points and obstacles in the Euclidean plane [1]. Each node in this graph models a point location, and each edge represents a visible connection between them. Applications of classical visibility graph theory included principally robot motion planning, geography, urban planning, and architecture [2]. In recent years, this paradigm was extended to the realm of time series analysis by looking at time series as finite samplings of one-dimensional landscapes. In this context, visibility and horizontal visibility graphs were introduced as a family of mappings between ordered sequences and graphs [3,4]. Consider an ordered sequence $\{\mathbf{x}(t)\}_{t=1}^{N}$, where $\mathbf{x}(t) \in \mathbb{R}^m$, $m \geqslant 1$. For $m = 1$, the sequence of $N$ data can for instance represent a univariate time series trajectory describing the activity of a complex system, such as the time evolution of a temperature, a stock price asset, or a heart interbeat measurement. Such dynamical information is subsequently mapped into a graph of $N$ nodes where any two nodes are linked in the graph if a particular visibility criterion [defined in Sec. II, cf. Eqs. (1) and (2) below] holds in the sequence (when $m > 1$, we get multivariate time series associated to high-dimensional dynamics [5]). This mapping thereby establishes the framework for the combinatorial description of dynamics and enables the possibility of performing graph-theoretical time series analysis by building a bridge between the theories of dynamical systems, signal processing, and graph theory.

In recent years, this mapping has been used to provide a topological characterization of different routes to low-dimensional chaos [6–8], or different types of stochastic and chaotic dynamics [9]. From an applied angle, it is being widely used to extract in a simple and computationally efficient way informative features for the description and classification of empirical time series in several areas of physics, including optics [10], fluid dynamics [11–13], geophysics [14], or astrophysics [15,16], and extend beyond physics in areas such as physiology [17,18], neuroscience [19], or finance [20]. Whenever each element in a given classification task is naturally encoded as an ordered sequence, one can map such sequence into a visibility graph and subsequently extract a certain set of topological properties of these graphs as the feature vector with which to train classifiers in supervised learning tasks.

Here, we extend this methodology from time series $\{\mathbf{x}(t)\}_{t=1}^{N}$ to scalar fields $h(x,y) : \mathbb{R}^d \to \mathbb{R}$. This extension has only been scarcely explored [21] and is conceptually closer to the original context of visibility graphs [1,2]. It enables the possibility of constructing the visibility graphs of images, landscapes, and general large-scale spatially extended surfaces. In what follows, we will introduce the concept along with a few definitions and properties. In Sec. III we provide analytical results on some topological properties of these graphs associated to some types of real-valued matrices which can be understood as the high and low disorder limits of real-valued scalar fields. In particular, we find a closed expression for the degree distribution of these graphs associated to uncorrelated random fields of generic dimension, extending the result known for one-dimensional time series. We show that this result, by holding independently of the field's marginal distribution, directly yields a statistical randomness test, applicable in arbitrary dimensions. In Sec. IV, we showcase its usefulness by discriminating two-dimensional white noise from two-dimensional lattice of diffusively coupled chaotic maps (a system that generated high-dimensional spatiotemporal chaos). In Sec. V, we discuss the range of potential applications of this combinatorial framework and we further briefly illustrate its usefulness for characterizing the process of oncogenesis through cell surface image analysis.

*l.lacasa@qmul.ac.uk
†j.iacovacci@qmul.ac.uk

 

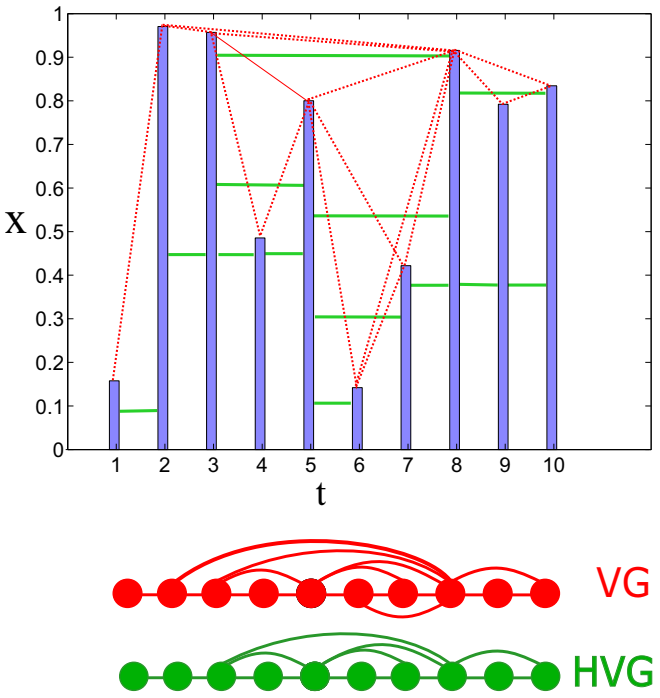


FIG. 1. Illustration of a sample time series and the construction of the associated horizontal visibility graph (HVG) and visibility graph (VG) following the definition and criteria given by Eqs. (1) and (2).

## II. DEFINITIONS AND BASIC PROPERTIES

We start by recalling the basic definition of visibility graphs (VG) and horizontal visibility graphs (HVG) (see [3,4] and Fig. 1 for an illustration):

*Definition* (VG). Let $\mathcal{S} = \{x_1, \ldots, x_N\}$ be an ordered sequence of $N$ real-valued, scalar data points. A visibility graph (VG) is an undirected graph of $n$ nodes, where each node $i \in [1, N]$ is labeled by the time order of its corresponding datum $x_i$. Hence, $x_1$ is mapped into node $i = 1$, $x_2$ into node $i = 2$, and so on. Then, two nodes $i$ and $j$ (assume $i < j$ without loss of generality) are connected by a link if and only if one can draw a straight line connecting $x_i$ and $x_j$ that does not intersect any intermediate datum $x_k$, $i < k < j$. Equivalently, $i$ and $j$ are connected if the following *convexity* criterion is fulfilled:

$$x_k < x_i + \frac{k-i}{j-i}[x_j - x_i], \quad \forall\, k : i < k < j. \tag{1}$$

The same definition applies to a horizontal visibility graph (HVG) [4] but in this latter graph two nodes $i, j$ (assume $i < j$ without loss of generality) are connected by a link if and only if one can draw a *horizontal* line connecting $x_i$ and $x_j$ that does not intersect any intermediate datum $x_k$, $i < k < j$. Equivalently, $i$ and $j$ are connected if the following *ordering* criterion is fulfilled:

$$x_k < \inf(x_i, x_j), \quad \forall\, k : i < k < j. \tag{2}$$

From a combinatoric point of view, HVGs are outer-planar graphs with a Hamiltonian path [22], i.e.. noncrossing graphs as defined in algebraic combinatorics [23]. Note that the former definitions focus on *discrete* sequences, such that the index labeling is such that $i + 1 \equiv i + \Delta$, where $\Delta$ is the spacing between data. Interestingly, both VG and HVG are invariant under changes in $\Delta$. Intuitively, this suggests that, in order to consider the *continuous* version of a discrete time series, one simply needs to take the limit $\Delta \to 0$. This invariance property in principle allows treating continuous scalar fields as the $\Delta \to 0$ limit of matrices, something that will be discussed later.

*Extension classes.* One can now extend the definition of visibility to handle two-dimensional manifolds, by simply extending the visibility criteria along one-dimensional sections of the manifold. The question is, in how many different ways one can do that? As a matter of fact, there exist several possibilities; here we consider just a few of them. We first consider manifolds of dimension $d$ which have a natural Euclidean embedding and define two extension classes, which we label as *canonical* and *fcc* respectively (incidentally, the name fcc is only loosely inspired in the face-centered cubic crystal shape). In the canonical extension class, the rule of thumb for extending the definition of a visibility graph to a manifold of dimension $d$ will be by applying the VG or HVG to $d$ orthogonal sections of the manifold (which define $n = 2d$ directions). In other words, at each point of the manifold, one constructs the VG or HVG in the direction of the (canonical) Cartesian axis. On the other hand, the fcc extension class allows an additional number of sections in the direction of the main diagonals. Accordingly, in this second class the number of directions is $n = 2d + 2^d$ directions (see Fig. 2 for an illustration in the case $d = 2$). Finally, a third extension class (which in this work will only be defined for $d = 2$ flat surfaces) is defined by taking $n$ directions in such a way that the set of $n$ vectors make a homogeneous angular partition of the plane with constant angle $2\pi/n$. This class is labeled as the order-$n$ class. Obviously, the order-8 and order-4 classes coincide, when $d = 2$, with the fcc and canonical classes, respectively, but they differ otherwise. These special classes are indeed of special relevance as they are perhaps the most natural algorithmic implementation for image processing. We are now ready to give a more formal definition of visibility graphs in these extension classes.

*Definition* (IVG$_n$). Let $\mathcal{I}$ be a $N \times N$ matrix, where $\mathcal{I}_{ij} \in \mathbb{R}$ and $N > 0$ (note at this point that $n$ and $N$ denote two different things). For an arbitrary entry $ij$, make an angular partition of the plane into $n$ directions, such that direction labeled as $p$

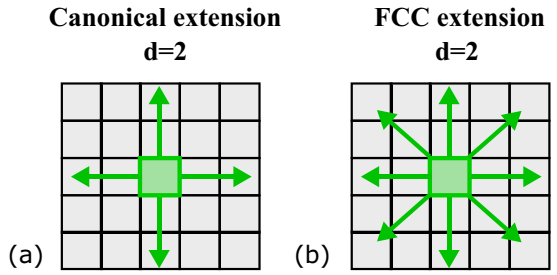


FIG. 2. Illustration of two extension classes of visibility algorithms in a dimension $d = 2$ data set (gray box matrix). In the canonical extension (a) for a given datum (green box) a visibility algorithm is evaluated along the vertical and horizontal directions. In the fcc extension (b) visibility is considered also along the diagonals crossing the green box.

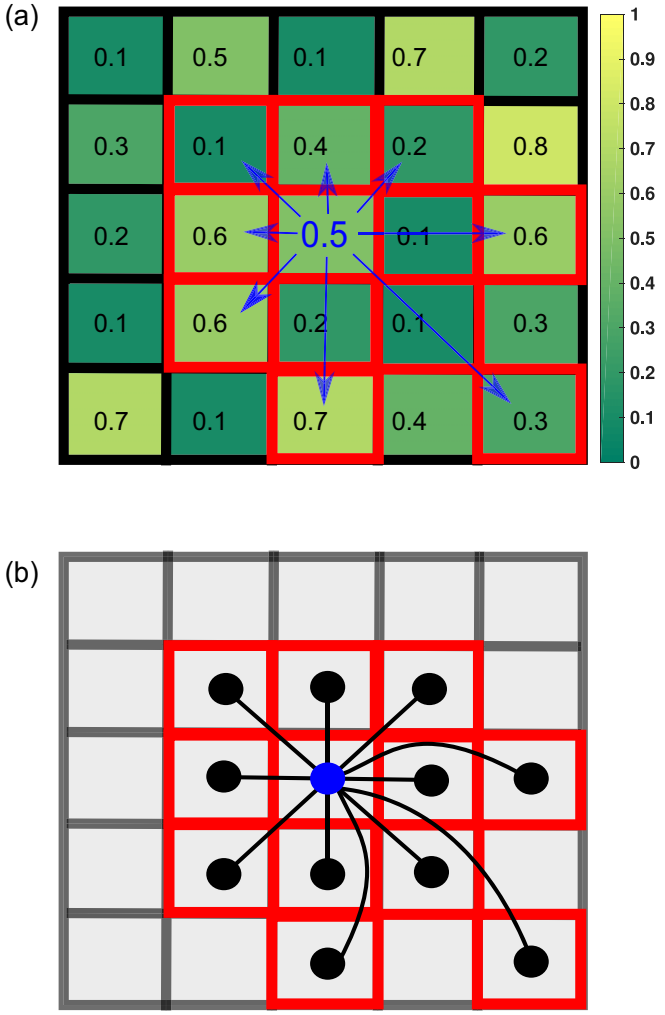


FIG. 3. Illustration of the $\mathrm{IHVG}_8$ construction. (a) Plots a sample square matrix, where the central entry in the matrix is selected (with value 0.5). Horizontal visibility criterion [Eq. (2)] along four lines (fcc extension class, blue arrows) is then applied to select visible data points over the image and field (red boxed pixels). (b) The connectivity pattern of the node associated to the selected entry is shown. By sequentially applying the algorithm to all the pixels in the matrix, the corresponding $\mathrm{IHVG}_8$ can be fully determined. To obtain the connectivity patterns of that node within $\mathrm{IVG}_8$ instead, one only needs to switch the linking criterion from Eq. (2) to Eq. (1).

makes an angle with the row axis of $2\pi(p-1)/n$. The *image visibility graph of order n* $\mathrm{IVG}_n$ is a graph with $N^2$ nodes, where each node is labeled by a duple $ij$ in association with the indices of the entry $\mathcal{I}_{ij}$, such that two nodes $ij$ and $i'j'$ are linked if

(1) $i'j'$ belongs to one of the $n$ angular partition lines, and

(2) $\mathcal{I}_{ij}$ and $\mathcal{I}_{i'j'}$ are linked in the VG defined over the ordered sequence which includes $ij$ and $i'j'$.

The *image horizontal visibility graph* ($\mathrm{IHVG}_n$) follows equivalently if in the second condition we make use of HVG instead of VG. For illustration, in Fig. 3 we depict a sample matrix [Fig. 3(a)] where we have highlighted the central entry, and in Fig. 3(b) of the same figure we describe the connectivity pattern associated to this entry in the case of $\mathrm{IHVG}_8$ [to obtain the connectivity patterns of that node within $\mathrm{IVG}_8$ instead, one only needs to switch the linking criterion from Eq. (2) to Eq. (1)].

Note that in the preceding definition, $\mathcal{I}$ can be understood as a two-dimensional square lattice, which is naturally embedded in $\mathbb{R}^2$ if we associate a certain lattice length $\Delta_p > 0$ to the separation between any two neighbors in each direction $p$. Since a two-dimensional square lattice is *coarsely equivalent* to $\mathbb{R}^2$, in the limit $N \to \infty$, $\Delta_p \to 0$ this matrix $\mathcal{I}$ converges in some mathematically well-defined sense to a continuous scalar field $h(x,y) : \mathbb{R}^2 \to R$. Accordingly, the continuous version of these graphs can be obtained for $n \to \infty$, and in that case $\mathrm{I(H)VG}_\infty$ would be an infinite graph. In this work, we keep $n$ finite and from now on only consider finite discretizations of scalar fields, however, the infinite case is certainly of theoretical interest and is left for future investigations.

For a given dimension $d$, one can define in a similar fashion the visibility graphs in the canonical extension class labeled $\mathrm{IVG}^c(\mathrm{d})$ by modifying condition (1): $i'j'$ belongs to one of the $d$ Cartesian axes which span $\mathbb{R}^d$ and have origin in $ij$. Analogously, the visibility graphs in the fcc extension class $\mathrm{IVG}^{\mathrm{fcc}}(\mathrm{d})$ are obtained by modifying again condition (1) appropriately to allow visibility in the main diagonals. Finally, again the horizontal version follows equivalently if in the second condition we make use of HVG instead of VG.

A trivial but important remark is that $\forall\, \mathcal{I}$, $\mathrm{I(H)VG}_4 = \mathrm{I(H)VG}^c(2)$ and $\mathrm{I(H)VG}_8 = \mathrm{I(H)VG}^{\mathrm{fcc}}(2)$. Note also that the special class $\mathrm{IVG}^c(2)$ has been explored recently under the name row-column visibility graph [21]. Once any of these graphs has been extracted from a given matrix $\mathcal{I}$, one can further compute standard topological properties on this graph using classical measures from graph theory [24] or recent metrics defined in network science [25], which in turn might be used to provide a topological characterization of $\mathcal{I}$. For instance, the degree $k$ of a node is the number of links of that node. This allows to construct the degree matrix $\mathbf{K} \in \mathbb{N}^{N\times N}$, where $\mathbf{K}_{ij}$ is the degree of node labeled with the pair $i,j$. The degree distribution $P(k)$ determines the probability of finding a node of degree $k$ and can be straightforwardly computed from the degree matrix. In this work for concreteness we will only consider these metrics, however, we should emphasize here that a large toolbox of measures could be used for feature extraction in context-dependent applications. Here, we are motivated to use these very simple metrics as it has recently been proved that, in the one-dimensional case, the set of degrees is on bijection with the adjacency matrix and hence is indeed an optimal feature [26].

In what follows, we depict some exact results on the topology of these graphs associated to simple types of matrices which can be understood as the high order and high disorder limits of real images. From now on we only consider the horizontal version of the visibility criteria, and we assume $N \to \infty$ to avoid border effects.

## III. SOME EXACT RESULTS

### A. Periodicity: Monochromatic images and chess boards

We start by considering trivial configurations at the end of total order. For monochromatic images where $\mathcal{I}_{ij} = c$, the $\mathrm{IHVG}_n$ is such that $\mathbf{K}_{ij} = n$ and thus $P(n) = 1$ and

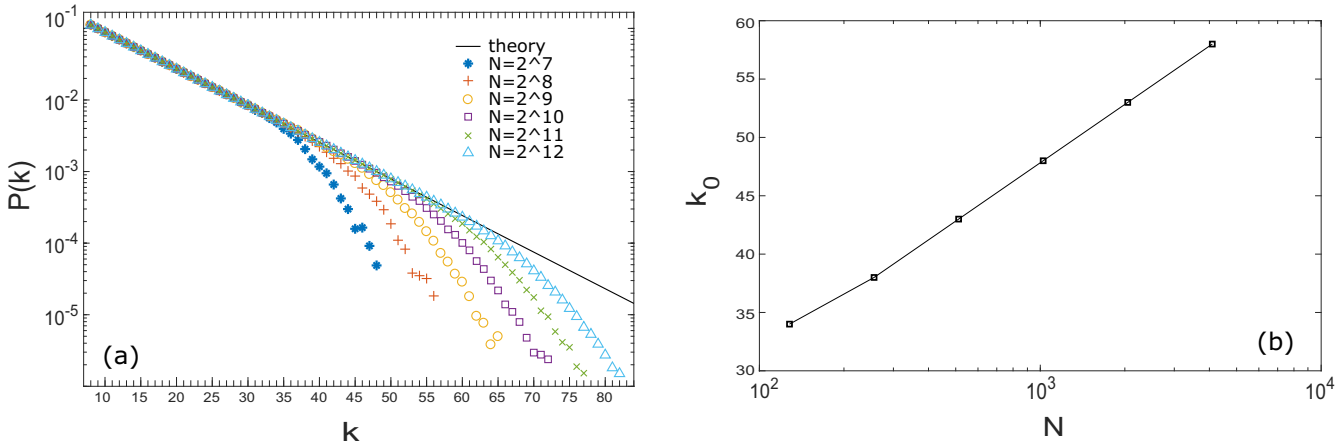


FIG. 4. (a) Semi-log plot of the degree distribution (ensemble averaged over 10 realizations) of IHVG$_8$ associated to $N \times N$ matrices with i.i.d. uniform U[0,1]random entries, for $N = 2^7, 2^8, \ldots, 2^{12}$. The solid line is the theoretical value of $P(k)$ given by Eq. (3) for $n = 8$. In every case we find excellent agreement for $k < k_0$, where $k_0$ is a cutoff value that denotes the onset of finite size effects. (b) Linear-log plot of the cutoff $k_0$ as a function of the system's size $N$ for the same data of (a), suggesting a logarithmic scaling $k_0 \sim c \log N$.

$P(k \neq n) = 0$. Then, we can consider chess boards. This is a periodic lattice, where in each row the same periodic sequence is represented (black, white, black, ...) $\equiv (1,-1,1,-1,\ldots)$, except for a one-step translation in even rows. Accordingly, neglecting boundary conditions $\mathcal{I}_{ij} = 1$ if $i \cdot j$ is odd and $-1$ otherwise. For IHVG$_4$ we find $\mathbf{K}_{ij} = 8$ if $i \cdot j$ is odd and 4 otherwise. For IHVG$_8$ we find $\mathbf{K}_{ij} = 12$ if $i \cdot j$ is odd and 8 otherwise. From this latter matrix the degree distribution is simply $P(k) = \frac{1}{2}$ for $k = 8,12$ and zero otherwise. For other types of periodic structures it is easy to see that the degree matrix will inherit such periodicity and thus the degree distribution will only be composed by a finite number $q$ of non-null probabilities, where $q$ in turn is typically bounded by a function that depends on the period of the periodic structure.

### B. Uncorrelated random fields

We then consider a limit configuration at the end of total disorder: a two-dimensional uncorrelated random field, i.e., white noise. Then, the following theorem holds for the degree distribution of IHVG$_n$:

*Main theorem*. Consider an $N \times N$ matrix with entries $\mathcal{I}_{ij} = \xi$, where $\xi$ is a random variable sampled from a distribution $f(x)$ with continuous real support $x \in (a,b)$. Then, for $n > 0$ and in the limit $N \to \infty$ the degree distribution of the associated IHVG$_n$ converges to

$$P(k) = \begin{cases} \left(\frac{1}{n+1}\right)\left(\frac{n}{n+1}\right)^{k-n}, & \text{if } k \geqslant n \\ 0, & \text{otherwise.} \end{cases} \quad (3)$$

For the sake of readability, the proof of this theorem has been put in an Appendix. A few comments are in order. First, note that this equation reduces, for $n = 2$ $(d = 1)$, to the well-known result for time series of i.i.d. variables $P(k) = (1/3)(2/3)^{k-2}$ [4]. Second, in the specific class $n = 8$ (equivalent to the fcc class in $d = 2$), Eq. (3) yields

$$P(k) = \begin{cases} \left(\frac{1}{9}\right)\left(\frac{8}{9}\right)^{k-8}, & \text{if } k \geqslant 8 \\ 0, & \text{otherwise.} \end{cases} \quad (4)$$

Third, note that in the limit of large $n$ we would have a continuous visibility scanning. The extension for any generic $n$ can also be directly interpreted as a generalization to higher-dimensional (discrete) scalar fields, so it is easy to show that Eq. (3) also applies to the degree distribution of (i) the canonical extension for dimension $d = n/2$ (i.e., only even values of $n$ are allowed in this case), and (ii) the fcc extension for dimension $d$, where $n = 2d + 2^d$ (i.e., for $n = 8,14,24,42,\ldots$). We are now ready to provide the proof of the theorem.

*Finite size effects*. To assess the convergence speed to Eq. (3) for finite $N$, we have estimated the degree distribution of IHVG$_8$ associated to $N \times N$ random matrices whose entries are i.i.d. uniform random variables U[0,1]. In Fig. 4 we plot, in semi-log scales, the resulting (finite size) degree distributions, for different $N = 2^7, 2^8, \ldots, 2^{12}$. As we can see, the distributions are in excellent agreement with Eq. (3) for $k \leqslant k_0$, where the location of the cutoff value $k_0$ scales logarithmically with the system's size $N$ as shown in the bottom of the figure. In other words, finite size effects only affect the tail of the distribution, which converges logarithmically fast with $N$.

## IV. A SIMPLE APPLICATION

The results for uncorrelated random fields found in the previous section are indeed of practical interest because Eq. (3) holds independently of the noise marginal distribution $f$. Resorting to the contrapositive, if the degree distribution of IHVG$_n$ deviates from Eq. (3) for some empirical field $\mathcal{I}$, one can conclude that the field is not uncorrelated noise. This theorem thereby allows for the straightforward design of a randomness statistical test which would be applicable to data structure of arbitrary dimension $d$, where $n(d) = 2d$ if one uses the canonical extension class, or $n(d) = 2d + 2^d$ in the case of fcc.

*Coupled map lattices*. To illustrate this, we consider a simple application of discriminating noise from high-dimensional chaos. Chaotic processes display irregular and unpredictable behavior which is often confounded with randomness, how-

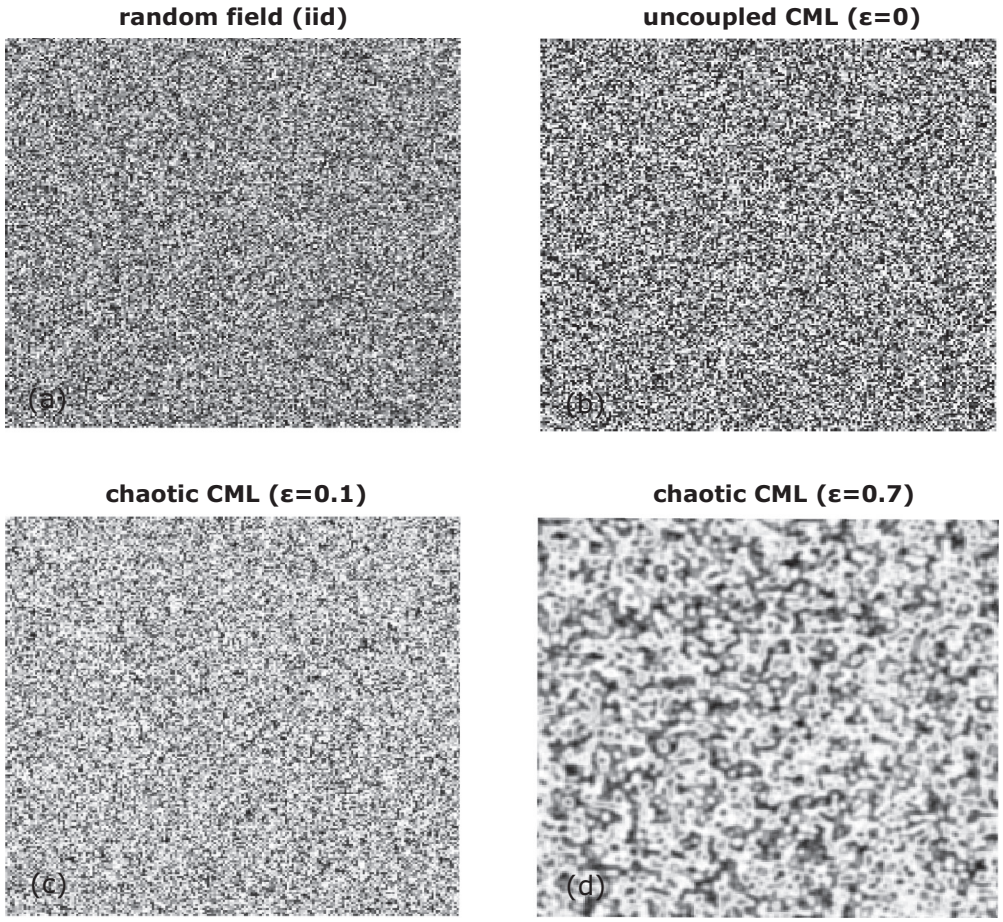


FIG. 5. Gray scale plots of $200 \times 200$ matrices describing (a) i.i.d. uniform U[0,1] random variables (uniform white noise); (b) a snapshot of a two-dimensional lattice of diffusively coupled chaotic logistic maps with coupling strength $\epsilon = 0$ (effectively being uncoupled and therefore a snapshot of uncorrelated beta distributed white noise); (c) the same coupled map lattice for weak coupling $\epsilon = 0.1$ for which the system displays fully developed turbulence (a state of spatiotemporal chaos with a high-dimensional attractor); (d) the same coupled map lattice for strong coupling $\epsilon = 0.7$. In this latter case the system shows strong spatial correlations and is easily distinguishable from the rest.

ever, chaos is a deterministic process which indeed hides in some cases some patterns that can be extracted by appropriate techniques. The endeavor of distinguishing noise from chaos has been an area of intense research activity in the last decades [27] and applications have pervaded nearly every scientific discipline where complex, irregular empirical signals emerge. Here, we consider spatially extended structures and thus we will be dealing with spatiotemporal chaos, i.e., chaotic behavior in space and in time, and we will explore whether visibility graphs are able to distinguish such dynamics from simple randomness. Let us define $\mathcal{I}(t)$ as a two-dimensional square lattice of $N^2$ diffusively coupled chaotic maps which evolve in time [28]. In each vertex of this coupled map lattice (CML) we allocate a fully chaotic logistic map $x_{t+1} = Q(x_t)$, $Q(x) = 4x(1-x)$, and the system is then spatially coupled as it follows:

$$\mathcal{I}_{ij}(t+1) = (1-\epsilon)Q[\mathcal{I}_{ij}(t)] + \frac{\epsilon}{4}\sum_{i',j'} Q[\mathcal{I}_{i'j'}(t)], \qquad (5)$$

where the sum extends to the Von Neumann neighborhood of $ij$ (four adjacent neighbors). The update is parallel and we use periodic boundary conditions. The coupling strength $\epsilon \in [0,1]$. For $\epsilon = 0$ the system is uncoupled and the $N^2$ logistic maps evolve independently. For positive $\epsilon > 0$, there is a balance between the internal (chaotic) dynamics which drives a local tendency towards inhomogeneity and the diffusion term (in the right hand of the equation one can easily recognize the discrete version of the Laplacian) which induces a global tendency towards homogeneity in space. This balance is tuned by $\epsilon$, acting as an effective viscosity constant, and the system evolves into different spatiotemporal dynamics as $\epsilon$ varies. For a small yet positive value of the coupling, the system displays so-called fully developed turbulence, a phase with incoherent spatiotemporal chaos and high-dimensional attractor [28]. In other words, the system evolves both temporally and spatially in a very irregular way, yet it is not totally uncorrelated. For illustration, in Fig. 5 we plot, for $N = 200$, gray scale *snapshots* of this system for $\epsilon = 0$ (uncoupled), $\epsilon = 0.1$ (weak coupling), and $\epsilon = 0.7$ (strong coupling) along with a $200 \times 200$ matrix of U[0,1] i.i.d. random variables (white noise). Note that the snapshot of the uncoupled case reduces to a collection of independent and identically distributed chaotic variables with a marginal distribution that coincides with the invariant measure of the fully chaotic logistic map: the beta distribution $\mathbb{B}(1/2,1/2) = \pi^{-1}x^{-1/2}(1-x)^{-1/2}$. In other words, such a snapshot is indistinguishable from

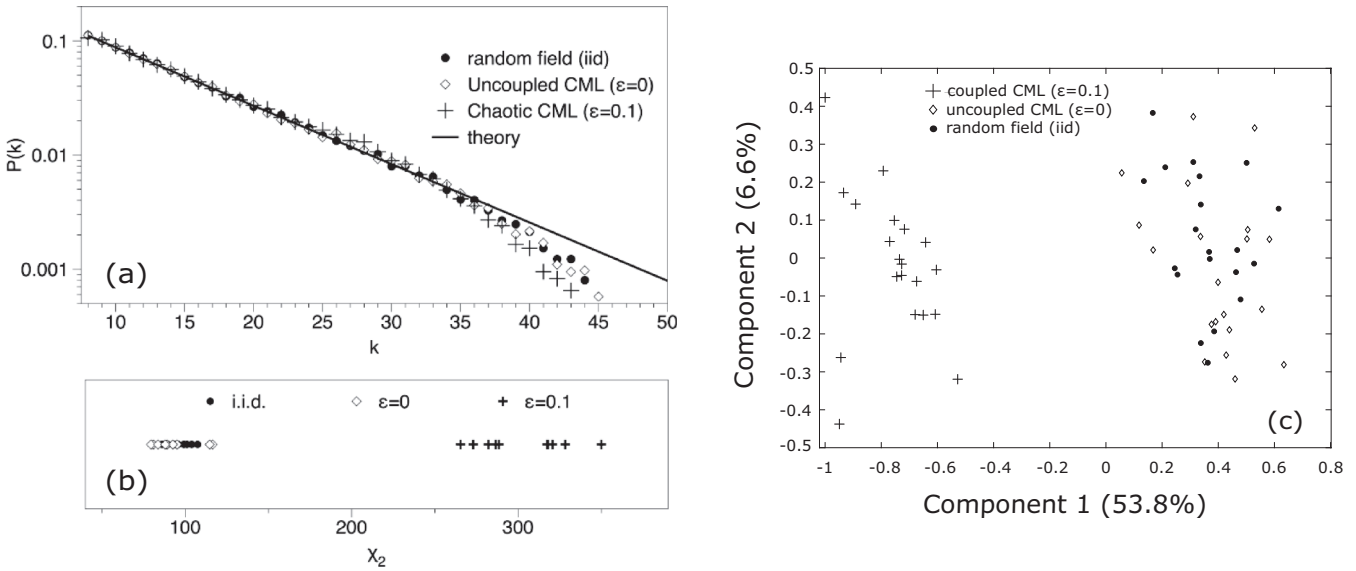


FIG. 6. (a) Semi-log plot of the degree distribution of $IHVG_8$ associated to a two-dimensional uncorrelated random field of uniform random variables (black dots), and two-dimensional coupled map lattices of diffusively coupled fully chaotic logistic maps, for coupling constant $\epsilon = 0$ (diamonds) and $\epsilon = 0.1$ (crosses). The solid line is Eq. (3) for $n = 8$. Deviations from the exponential law in the tail are due to finite size effects (in every case matrices are $200 \times 200$). Note that the $\epsilon = 0$ case is effectively a spatially uncorrelated field with i.i.d. entries (with marginal distribution equivalent to the invariant measure of an isolated logistic map, i.e., the beta distribution). For $\epsilon = 0.1$ the system is weakly coupled and displays fully developed turbulence (spatiotemporal chaos with high-dimensional attractor, i.e., the snapshot is weakly correlated). All three snapshots [Figs. 5(a)–5(c)] look very similar and, expectedly, they all display *apparently similar* degree distributions. (b) Here we consider 20 realizations of each of the three systems, and in each case compute the $\chi_2$ statistic (see the text) measuring the deviation of the empirical degree distribution ($k < 44$) from the theory for random fields. As expected, the i.i.d. cases (random field and snapshot of the uncoupled logistic maps) are indistinguishable, but the weakly coupled system is clearly distinguished, finding stronger deviations from Eq. (3) than those found due to finite size effects. (c) Principal component analysis (PCA) of the set of degree distributions for the 60 realizations explored in (b). Each degree distribution $P(k)$ has been projected in a two-dimensional space spanned by the first two principal components (this subspace accounts for 60% of the variability). One does not need to apply any clustering algorithm as the nonrandom matrices are very clearly clustered together and apart from the i.i.d. cases.

white, beta-distributed noise, which should be then equivalent under the IHVG mapping to any type of white noise and should therefore fulfill our theorem. When $\epsilon > 0$ spatial correlations settle in and the snapshots are in theory statistically different, however, this difference is only evident for large coupling.

*Distinguishing noise from chaos*. To explore such differences, we can exploit our theorem as it follows: first, we estimate the degree distribution of the $IHVG_8$ of each snapshot, and compare against the theoretical equation for white noise. To account for finite size effects, it is necessary to compare the estimation of the chaotic case not just with Eq. (3) but also with a finite i.i.d. sample. We have generated 20 realizations of each process (random uniform noise, $\epsilon = 0$ and 0.1) and have extracted the degree distribution of $IHVG_8$ for each case. Sample results of these distributions can be shown in Fig. 6(a) along with the theoretical prediction for i.i.d [Eq. (4)]. As expected, the distributions are *apparently* very well approximated by Eq. (4) in every case (there are strong deviations for $k > 35$ but this is due to finite size effects as similar deviations take place for the i.i.d. white uniform noise case). To quantify potential deviations from the theory (which according to the theorem would imply nonrandomness), for each case we have computed the $\chi^2$ statistic

$$\chi^2 = N \sum_k \frac{[P_{\rm th}(k) - P_{\rm exp}(k)]^2}{P_{\rm th}(k)},$$

where we have taken $k = 8, 9, \ldots, 44$. Results are shown in Fig. 6(b), showing now a clear separation between the uncorrelated cases (uncoupled chaotic maps and uniform white noise) and the weakly coupled system. This clear distinction is further confirmed in a principal component analysis (PCA) depicted in Fig. 6(c), where each degree distribution $P(k)$ has been projected in a two-dimensional space spanned by the first two principal components (this subspace accounts for 60% of the variability). One does not need to apply any clustering algorithm as the nonrandom matrices are very clearly clustered together and apart from the i.i.d. cases.

*Phase diagram*. As mentioned previously, the spatiotemporal dynamics of the coupled map lattice shows a rich phase diagram as we increase the coupling constant $\epsilon$. An easy way of encapsulating and visualizing such richness in a single diagram is presented in Fig. 7(a). For each $\epsilon$, we compute the degree distribution of the associated $IHVG_8$. Then, we compute the distance $D$ between the degree distribution at $\epsilon$ and the corresponding result for $\epsilon = 0$ [Eq. (4)] $D = \sum_k |P(k) - (1/9)(8/9)^{k-8}|$. $D$ acts as a scalar order parameter describing the spatial configuration of the CML and, interestingly, evidences sharp changes for the different phases, such as for $\epsilon < 0.12$, the system develops fully developed turbulence (FDT) with weak spatial correlations. This regime shifts to a periodic structure (PS) for $0.12 < \epsilon < 0.27$. This regime then parsimoniously shifts into a phase with spatially

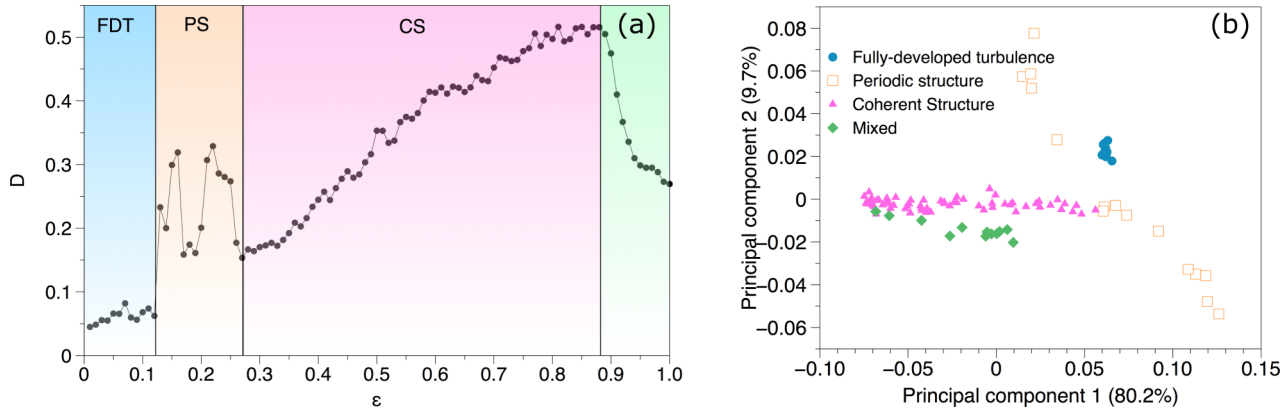


FIG. 7. (a) Scalar parameter $D$ (see the text) as a function of the coupling constant $\epsilon$, computed from the degree distribution of $IHVG_8$ associated to $100 \times 100$ CMLs of fully chaotic logistic maps. $D$ captures the spatiotemporal phases: fully developed turbulence (FDT), periodic structure (PS), coherent structure (CS), and a mixed phase. Snapshots characteristic of these phases are depicted in Fig. 9 in an Appendix. (b) Principal component analysis (PCA) of the degree distributions of $IHVG_8$ associated to the same data of (a). The plot is a projection into the first two principal components (accumulating over 90% of the data variability). The different heuristic phases are highlighted.

coherent structures (CS), which ultimately break down for $\epsilon > 0.88$ in favor of periodic patterns. For $0.88 < \epsilon < 1$ the spatial structure shows a mix between CS and PS. We conclude that the degree distribution of the $IHVG_8$ captures this rich spatial structure, something confirmed via principal component analysis in Fig. 7(b).

## V. DISCUSSION

This framework allows the possibility of describing discretized scalar fields of arbitrary origin in a combinatorially compact fashion, and enables using the tools of graph theory and network science for the practical description and classification of spatially extended data structures. For the sake of exposition and concreteness, in this work we have only used a couple of graph measures (degree matrix and degree distribution) which can be argued that were optimal in the one-dimensional case [26], but it should be highlighted that this method is much more general and allows to extract from these graphs any desired property.

For $d = 1$ the method was naturally designed for the task of time series analysis, and has been exploited accordingly and extensively in the last years, both from a theoretical point of view and for applications, as was acknowledged in the Introduction section. Here, we have presented a natural extension of these algorithms to deal with (discretized) scalar fields of arbitrary dimension, along with a few exact results on simple, yet relevant, cases. From a mathematical point of view, the task of characterizing the graphs in these extension classes provides a wide range of challenging open questions, which could parallel recent advancements in the one-dimensional case [9]. Now, what are the potential *applications* of this framework?

For $d = 2$ (either using the canonical or fcc extension classes, or the order-$n$ class), a plethora of applications emerge, here we only enumerate and discuss a few: (i) *Image processing*: A (gray scale) image is just a discrete scalar field. Once we extract the visibility graphs of a given image, can we use the topological properties of this graph to build feature vectors which can feed automatic classifiers for several statistical learning tasks involving images [29]? Can we define the distance between two images using graph kernels [30] on the associated visibility graphs? (ii) *Physics of interfaces*: Can we provide a topological characterization of fractal surface growth [31]? Can we, for instance, account for spatial self-similar structures much in the same way the Hurst exponent of fractional Brownian motion was estimated with visibility graphs [32] (a preliminary analysis via row-column visibility graphs has partly addressed this issue recently [21]). Furthermore, can we apply this methodology in biologically relevant problems and beyond, for instance, to classify tumoral or calli surfaces? (iii) *Urban planning*: Can we automatically cluster cities by only resorting to combinatorial properties extracted from their visibility graphs? And can we link such emerging clusters with architectural, historical, or cultural properties of cities? (iv) *Random matrix theory*: Is there a visibility graph characterization of different random matrix ensembles?

To illustrate the potential applicability of the method to the case of tumor description, in Fig. 8(d) we plot the degree distribution of the $IHVG_8$ associated to three atomic force microscopy (AFM) images ($94 \times 94$ after gray scale preprocessing) of normal [Fig. 8(a)], immortal [premalignant, Fig. 8(b)], and cancer [malignant, Fig. 8(c)] cervical epithelial cells [33]. This very preliminary evidence suggests that the carcinogenesis transition normal $\rightarrow$ premalignant $\rightarrow$ cancer is paralleled in $IHVG_8$ graph space by a systematic deviation of the degree distribution from the i.i.d. case. In Figs. 8(e)–8(g) we plot the degree distributions associated to $IVG_8$ instead, whose tails have been fitted to exponential functions $\sim\exp(-\lambda k)$. We find that exponents seem to change during carcinogenesis as $\lambda_{\text{normal}} < \lambda_{\text{immortal}} < \lambda_{\text{cancer}}$ [34]. These are of course very preliminary results given simply for illustration, and future research should confirm their accuracy and their potential use for carcinogenesis description and early detection.

The most exciting application for higher dimensions $d \geqslant 2$ is perhaps on describing the spatial structure of generic energy landscapes [35] $V : \mathbf{x} \in \mathbb{R}^d \rightarrow \mathbb{R}$, where $d$ is the number of degrees of freedom. Typically, these fields describe an energy function whose minimum is associated to the macroscopic behavior of many-body systems, and play a major role

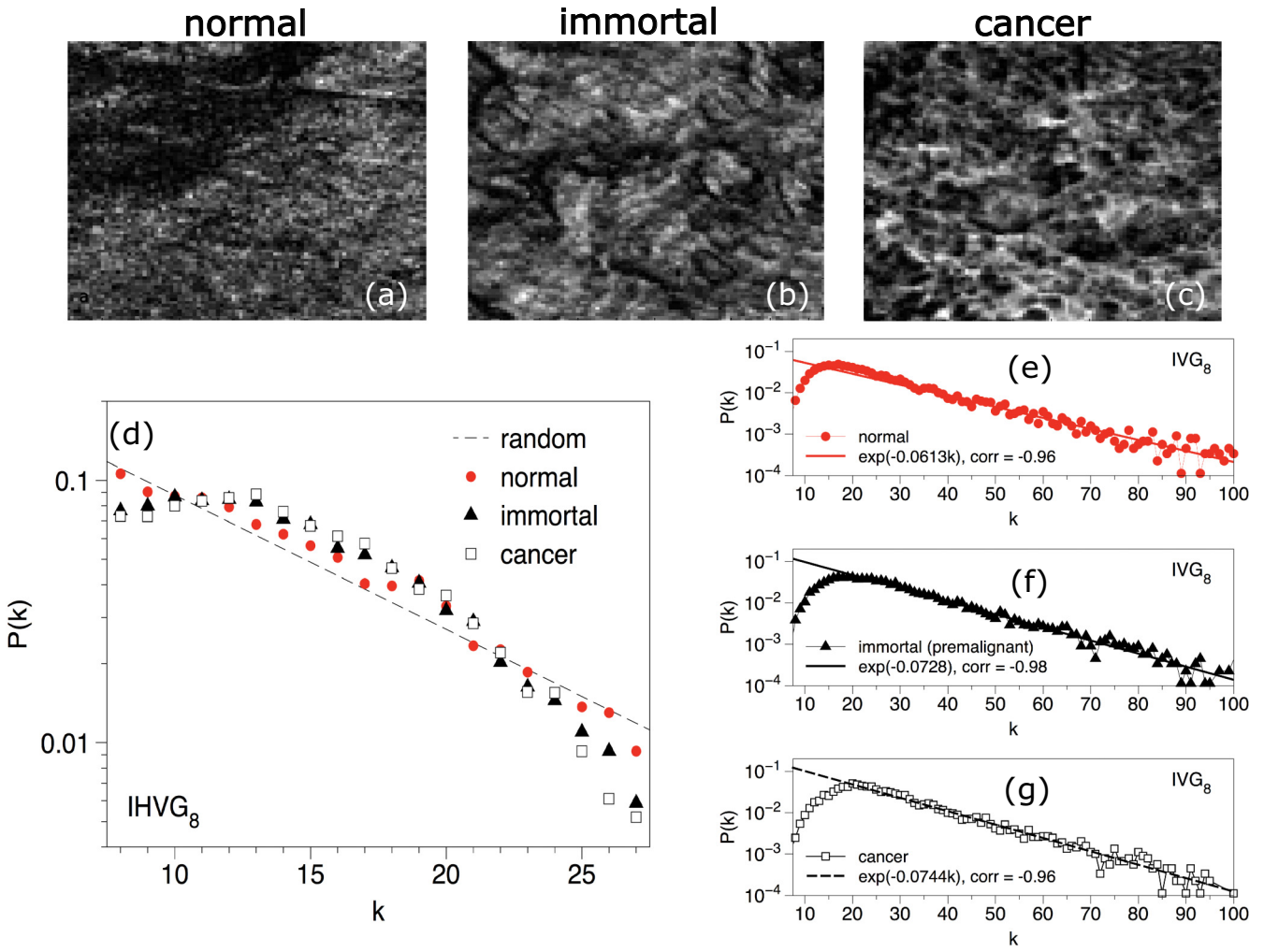


FIG. 8. (a)–(c) Gray scale atomic force microscopy images of normal (a), immortal (premalignant) (b), and cancer (malignant) (c) cervical epithelial cells (extracted from [33] after permission from Sokolov). (d) Semi-log plot of the degree distribution of $\mathrm{IHVG}_8$ associated to the three images: normal (red dots), immortal (black triangles), and cancerous (black hollow squares) cells [33]. Normal cells display a distribution closer to an uncorrelated random field [Eq. (3) for $n = 8$], and this preliminary evidence suggests that the transition normal $\rightarrow$ immortal $\rightarrow$ cancer is paralleled by a systematic deviation from the random field case for most of the degrees $k$ in $P(k)$. (e)–(g) Analogous plot for the degree distributions in the case of $\mathrm{IVG}_8$. The distributions now have a clear exponential tail, and we have used least squares to fit exponential functions $\sim\exp(-\lambda k)$ to the tails of the distributions, i.e., in the range $k \geqslant 30$ (dispersion is Gaussian distributed, a requirement to use least-squares minimization). Fitting suggests $\lambda_{\mathrm{normal}} < \lambda_{\mathrm{immortal}} < \lambda_{\mathrm{cancer}}$, something that should be carefully validated in a larger study.

in physics and chemistry. The structure of these fields is, however, rather messy. As a matter of fact, in spin glasses and other disordered systems, their macroscopic properties do not necessarily relate directly to a configuration of minimal energy as the system gets trapped in local, metastable minima of this energy surface: in this sense the spatial distribution and overall structure of these minima (stationary points) gives valuable information on the system dynamical evolution. These energy surfaces are also of great interest in chemistry (Kramer's reaction rate theory for the thermally activated escape from metastable states) and high energy physics (e.g., local minima of supersymmetric energy landscape corresponds to the field theory vacuum). The formalism presented here would enable the description of such energetic landscapes, opening a thread of questions such as follows: Can we classify different types of field theories only using combinatorial criteria on their energy landscapes? What is the spatial distribution of stationary points of different canonical disordered systems in the light of this new method?

To conclude, we hopefully made the case that to encode spatially extended structures in a combinatorial fashion is an enterprise that opens exciting theoretical questions as well as applications. The approach presented here is promising and there exist several possible avenues for future research, and we hope that these methods spark interest in some of these communities accordingly.

## ACKNOWLEDGMENTS

We thank I. Sokolov for granting permission to reproduce the images on normal, immortal, and cancer cells. L.L. acknowledges funding from EPSRC Early Career Fellowship No. EP/P01660X/1. Codes available upon request.

## APPENDIX: PROOF OF THE MAIN THEOREM

The proof of the main theorem stated in Sec. III B essentially makes use of the diagrammatic formalism introduced in Refs. [4,9] where, in the case of time series, the probability of each degree was expanded in a series expansion of terms, each term associated to a different diagram and contributing with different amplitude. Let us start by considering the concrete case $n = 8$ (which describes the case implemented in our algorithm for image filtering) and we will generalize for all $n$ thereafter. Using the jargon developed in Refs. [4,9], a node chosen at random which has horizontal visibility of $k$ others can be modeled as a *seed* (contributing with probability $\mathfrak{S}$) which has visibility of $k-8$ *inner* nodes (contributing with $\mathfrak{I}$) distributed along the $n = 8$ directions (such that direction $i$ contributes with $k_i$ inner nodes), and whose visibility is finally bounded by eight *bounding* nodes (contributing with probability $\mathfrak{B}$). The probability that a node chosen at random has horizontal visibility of $k$ other nodes can thus be formally expressed as

$$P(k) = \sum_{\{k_1,k_2\ldots k_8\}} \mathfrak{S}\mathfrak{B}^8 \prod_{i=1}^{8} \mathfrak{I}_{k_i}, \tag{A1}$$

where the sum enumerates all admissible combinations of $\{(k_1,k_2,\ldots,k_8)\}$ such that $\sum_{i=1}^{8} = k-8$ (by construction, every node always has visibility of its boundary, here formed by $n = 8$ nodes). It is easy to see that a possible enumeration is

$$k_i = 0,1,\ldots,k-8-\sum_{m=1}^{i-1} k_m \quad \text{for } i = 1,2,\ldots,7;$$

$$k_8 = k-8-\sum_{i=1}^{7} k_i.$$

Making use of the cumulative distribution $F(x) = \int_a^x f(x')dx'$ [with $F(a) = 0$, $F(b) = 1$] and following [4,9], geometrically it is easy to see that

$$\mathfrak{S} = \int_a^b f(x_0)dx_0; \quad \mathfrak{B} = \int_{x_0}^b f(x)dx = 1-F(x_0).$$

To describe the probability of finding $p$ inner nodes $\mathfrak{I}_p$, by construction we shall take into account that an arbitrary number $r$ (from zero to an infinite amount) of *hidden* data (i.e., nodes that are not visible from the seed) can lie in-between every pair of aligned inner nodes. Such arbitrary number of hidden data should contribute with the following amplitude:

$$\sum_{r=0}^{\infty}\prod_{j=1}^{r}\int_a^x f(n_j)dn_j = \frac{1}{1-F(x)},$$

where we have used the properties of the cumulative distribution to find the last identity. Accordingly, the concatenation of $p$ inner data which might have an arbitrary number of interspersed hidden data can be expressed as

$$\mathfrak{I}_p = \int_a^{x_0} \frac{f(x_1)dx_1}{1-F(x_1)} \prod_{j=1}^{n-1}\int_{x_j}^{x_0} \frac{f(x_{j+1})dx_{j+1}}{1-F(x_{j+1})}. \tag{A2}$$

This latter calculation is easy but quite tedious. One proceeds to integrate Eq. (A2) step by step and a recurrence quickly becomes evident. One can easily prove by induction that

$$\mathfrak{I}_p = \frac{(-1)^p}{p!}\{\ln[1-F(x_0)]\}^p.$$

We are thus ready to tackle Eq. (A1). Taking advantage of the closure $\sum_{i=1}^{8} K_i = k-8$, we first have

$$\prod_{i=1}^{8}\mathfrak{I}_{k_i} = \frac{(-1)^{k-8}\{\ln[1-F(x_0)]\}^{k-8}}{\prod_{i=1}^{8}(k_i)!},$$

so after some reordering,

$$P(k) = \sum_{\{k_1,k_2\ldots k_8\}} \frac{(-1)^{k-8}}{\prod_{i=1}^{8}(k_i)!}\int_a^b f(x_0)[1-F(x_0)]^8 \times \{\ln[1-F(x_0)]\}^{k-8}dx_0.$$

Now, in this latter equation the integral is easy to compute:

$$\int_a^b f(x_0)[1-F(x_0)]^8\{\ln[1-F(x_0)]\}^{k-8}dx_0 = (-1)^{k-8}(k-8)!\left(\tfrac{1}{9}\right)^{k-7}.$$

Consider finally the term

$$\sum_{\{k_1,k_2\ldots k_8\}} \frac{(k-8)!}{\prod_{i=1}^{8}(k_i)!} = (k-8)!\sum_{k_1=0}^{k-8}\sum_{k_2=0}^{k-8-k_1}\cdots\sum_{k_7=0}^{k-8-\sum_{j=1}^{7}k_j} \frac{1}{k_1!}\frac{1}{k_2!}\cdots\frac{1}{k_7!}\frac{1}{\left(k-8-\sum_{j=1}^{7}k_j\right)!} = 8^{k-8}, \tag{A3}$$

where the last identity was found by iteratively applying the binomial theorem $\sum_{k=0}^{a}\binom{a}{k}r^k = (1+r)^a$. Altogether, we can write explicitly for $n = 8$

$$P(k) = \left(\tfrac{1}{9}\right)\left(\tfrac{8}{9}\right)^{k-8}$$

for $k \geqslant 8$ and zero otherwise. This result is independent of $f(x)$ as expected since HVG is an order statistic [36], and coincides with Eq. (3) for $n = 8$ [i.e., Eq. (4)].

We are now ready to generalize the whole derivation. For a generic $n$, trivially

$$P(k) = \sum_{\{k_1,k_2\ldots k_n\}} \frac{(-1)^{k-n}}{\prod_{i=1}^{n}(k_i)!}\int_a^b f(x_0)[1-F(x_0)]^n\{\ln[1-F(x_0)]\}^{k-n}dx_0$$

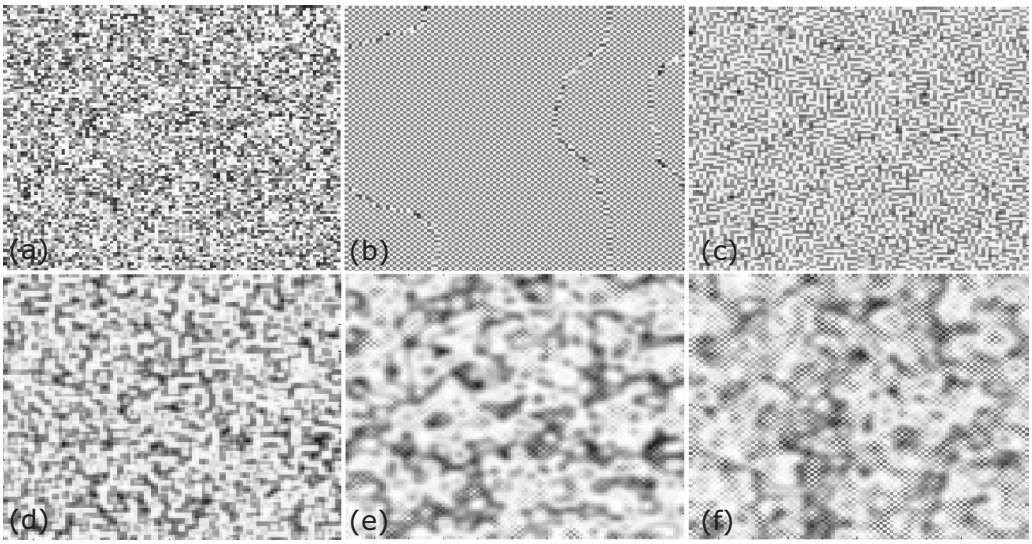


FIG. 9. Gray scale snapshot plots of $100 \times 100$ CMLs [Eq. (5)] for different values of $\epsilon$. From top left to bottom right, respectively: $\epsilon = 0.05$ [fully developed turbulence (a)], $\epsilon = 0.15$ and 0.25 [periodic structure (b) and (c), respectively], $\epsilon = 0.4$ and 0.8 [coherent structure (d) and (e), respectively], and $\epsilon = 0.95$ [coexistence state with both coherent and periodic structures intertwined (f)].

with

$$\int_a^b f(x_0)[1 - F(x_0)]^n \{\ln[1 - F(x_0)]\}^{k-n} dx_0 = \left(\frac{1}{n+1}\right)^{k-n+1} (-1)^{k-n}(k-n)!$$

such that

$$P(k) = \left(\frac{1}{n+1}\right)^{k-n+1} \sum_{\{k_1,k_2\ldots k_n\}} \frac{(k-n)!}{\prod_{i=1}^n (k_i)!}.$$

Finally, since

$$\sum_{\{k_1,k_2\ldots k_n\}} \frac{(k-n)!}{\prod_{i=1}^n (k_i)!} = n^{k-n},$$

we find

$$P(k) = \left(\frac{1}{n+1}\right)^{k-n+1} n^{k-n} = \left(\frac{1}{n+1}\right)\left(\frac{n}{n+1}\right)^{k-n},$$

which concludes the proof. ■

Note that a similar result can be found much more easily at the expense of using a nonrigorous heuristic argument. In the case $n = 8$, the probability that the seed node has visibility of exactly $k$ nodes can be expressed as the probability that there are $k - 8$ nodes that are not bounding times the probability that after these, the boundary prevents larger visibility. Accordingly, we shall write

$$P(k) = [1 - P(8)]^{k-8} P(8).$$

For $k = 8$, $k_i$ only takes the value $k_i = 0 \; \forall \; i = 1 \ldots 8$, hence, this term is straightforward to compute:

$$P(8) = \mathfrak{S}\mathfrak{B}^8 = \int_a^b f(x_0)\left[\int_{x_0}^b f(x)dx\right]^8 dx_0 = \frac{1}{9}, \; \forall \; f$$

which then yields the correct shape for $P(k)$:

$$P(k) = [1 - P(8)]^{k-8} P(8) = \left(\tfrac{1}{9}\right)\left(\tfrac{8}{9}\right)^{k-8}.$$

A similar argument can be used for a generic $n$, yielding

$$P(k) = [1 - P(n)]^{k-n} P(n) = \left(\frac{1}{n+1}\right)\left(\frac{n}{n+1}\right)^{k-n}$$

for $k \geqslant n$ and zero otherwise, in agreement with Eq. (3).

[1] M. de Berg, M. van Kreveld, M. Overmars, and O. Schwarzkopf, *Computational Geometry*, 2nd ed. (Springer, Berlin, 2000), pp. 307–317.

[2] A. Turner, M. Doxa, D. O'sullivan, and A. Penn, From isovists to visibility graphs: A methodology for the analysis of architectural space, Environ. Planning B: Planning Design **28**, 103 (2001).

[3] L. Lacasa, B. Luque, F. J. Ballesteros, J. Luque, and J. C. Nuno, From time series to complex networks: The visibility graph, Proc. Natl. Acad. Sci. USA **105**, 4972 (2008).

[4] B. Luque, L. Lacasa, J. Luque, and F. J. Ballesteros, Horizontal visibility graphs: Exact results for random time series, Phys. Rev. E **80**, 046103 (2009).

[5] L. Lacasa, V. Nicosia, and V. Latora, Network structure of multivariate time series, Sci. Rep. **5**, 15508 (2015).

[6] B. Luque, L. Lacasa, F. Ballesteros, and A. Robledo, Analytical properties of horizontal visibility graphs in the Feigenbaum scenario, Chaos **22**, 013109 (2012).

[7] B. Luque, A. Núñez, F. Ballesteros, and A. Robledo, Quasiperiodic graphs: Structural design, scaling and entropic properties, J. Nonlinear Sci. **23**, 335 (2012).

[8] A. M. Núñez, B. Luque, L. Lacasa, J. P. Gómez, and A. Robledo, Horizontal visibility graphs generated by type-I intermittency, Phys. Rev. E **87**, 052801 (2013).

[9] L. Lacasa, On the degree distribution of horizontal visibility graphs associated to Markov processes and dynamical systems: Diagrammatic and variational approaches, Nonlinearity **27**, 2063 (2014).

[10] A. Aragoneses, L. Carpi, N. Tarasov, D. V. Churkin, M. C. Torrent, C. Masoller, and S. K. Turitsyn, Unveiling Temporal Correlations Characteristic of a Phase Transition in the Output Intensity of a Fiber Laser, Phys. Rev. Lett. **116**, 033902 (2016).

[11] M. Murugesan and R. I. Sujith, Combustion noise is scale-free: Transition from scale-free to order at the onset of thermoacoustic instability, J. Fluid Mech. **772**, 225 (2015).

[12] A. Charakopoulos, T. E. Karakasidis, P. N. Papanicolaou, and A. Liakopoulos, The application of complex network time series analysis in turbulent heated jets, Chaos **24**, 024408 (2014).

[13] P. Manshour, M. R. Rahimi Tabar, and J. Peinche, Fully developed turbulence in the view of horizontal visibility graphs, J. Stat. Mech. (2015) P08031.

[14] R. Donner and J. F. Donges, Visibility graph analysis of geophysical time series: Potentials and possible pitfalls, Acta Geophys. **60**, 3 (2012).

[15] V. Suyal, A. Prasad, and H. P. Singh, Visibility-graph analysis of the solar wind velocity, Sol. Phys. **289**, 379 (2014).

[16] Y. Zou, R. V. Donner, N. Marwan, M. Small, and J. Kurths, Long-term changes in the north-south asymmetry of solar activity: A nonlinear dynamics characterization using visibility graphs, Nonlin. Process. Geophys. **21**, 1113 (2014).

[17] J. F. Donges, R. V. Donner, and J. Kurths, Testing time series irreversibility using complex network methods, Europhys. Lett. **102**, 10004 (2013).

[18] S. Jiang, C. Bian, X. Ning, and Q. D. Y. Ma, Visibility graph analysis on heartbeat dynamics of meditation training, Appl. Phys. Lett. **102**, 253702 (2013).

[19] M. Ahmadlou, H. Adeli, and A. Adeli, New diagnostic EEG markers of the Alzheimer's disease using visibility graph, J. Neural Transm. **117**, 1099 (2010).

[20] R. Flanagan and L. Lacasa, Irreversibility of financial time series: A graph-theoretical approach, Phys. Lett. A **380**, 1689 (2016).

[21] X. Qin, P. Xue, L. Xin-Li, M. Stephen, Y. Hui-Jie, J. Yan, W. Jian-Yong, and Z. Quin-Jun, Row-column visibility graph approach to two-dimensional landscapes, Chin. Phys. B **23**, 078904 (2014).

[22] S. Severini, G. Gutin, and T. Mansour, A characterization of horizontal visibility graphs and combinatorics on words, Phys. A (Amsterdam) **390**, 2421 (2011).

[23] P. Flajolet and M. Noy, Analytic combinatorics of non-crossing configurations, Discrete Math. **204**, 203 (1999).

[24] B. Bollobas, *Modern Graph Theory* (Springer, New York, 1998).

[25] M. Newman, *Networks: An Introduction* (Oxford University Press, Oxford, 2010).

[26] B. Luque and L. Lacasa, Canonical horizontal visibility graphs are uniquely determined by their degree sequence, Eur. Phys. J. Spec. Top **226**, 383 (2017)

[27] H. Kantz and T. Schreiber, *Nonlinear Time Series Analysis* (Cambridge University Press, Cambridge, 2000).

[28] K. Kaneko, Overview of coupled map lattices, Chaos **2**, 279 (1992).

[29] J. Iacovacci and L. Lacasa (unpublished).

[30] S. V. Vishwanathan, N. N. Schraudolph, R. Kondor, and K. M. Borgwardt, Graph kernels, J. Machine Learning Res. **11**, 1201 (2010).

[31] A. L. Barabasi and H. E. Stanley, *Fractal Concepts in Surface Growth* (Cambridge University Press, Cambridge, 1995).

[32] L. Lacasa, B. Luque, J. Luque, and J. C. Nuno, The visibility graph: A new method for estimating the Hurst exponent of fractional Brownian motion, Europhys. Lett. **86**, 30001 (2009).

[33] M. E. Dokukin, N. V. Guz, C. D. Woodworth, and I. Sokolov, Emerging of fractal geometry on surface of human cervical epithelial cells during progression towards cancer, New J. Phys. **17**, 033019 (2015).

[34] M. E. Dokukin, N. V. Guz, R. M. Gaikwad, C. D. Woodworth, and I. Sokolov, Cell Surface as a Fractal: Normal and Cancerous Cervical Cells Demonstrate Different Fractal Behavior of Surface Adhesion Maps at the Nanoscale, Phys. Rev. Lett. **107**, 028101 (2011).

[35] D. Wales, *Energy Landscapes: Applications to Clusters, Biomolecules and Glasses* (Cambridge University Press, Cambridge, 2004).

[36] L. Lacasa and R. Flanagan, Time reversibility from visibility graphs of non-stationary processes, Phys. Rev. E **92**, 022817 (2015).